SYNAPSE-Net: A Unified Framework with Lesion-Aware Hierarchical Gating for Robust Segmentation of Heterogeneous Brain Lesions

Md. Mehedi Hassan^{a,*}, Shafqat Alam^a, Shahriar Ahmed Seam^b, Maruf Ahmed^c

^aDepartment of Biomedical Engineering, Bangladesh University of Engineering and Technology, Dhaka, Bangladesh ^bDepartment of Computer Science and Engineering, Bangladesh University of Engineering and Technology, Dhaka, Bangladesh ^cDepartment of Electrical and Electronic Engineering, Bangladesh University of Engineering and Technology, Dhaka, Bangladesh

Abstract

Abstract

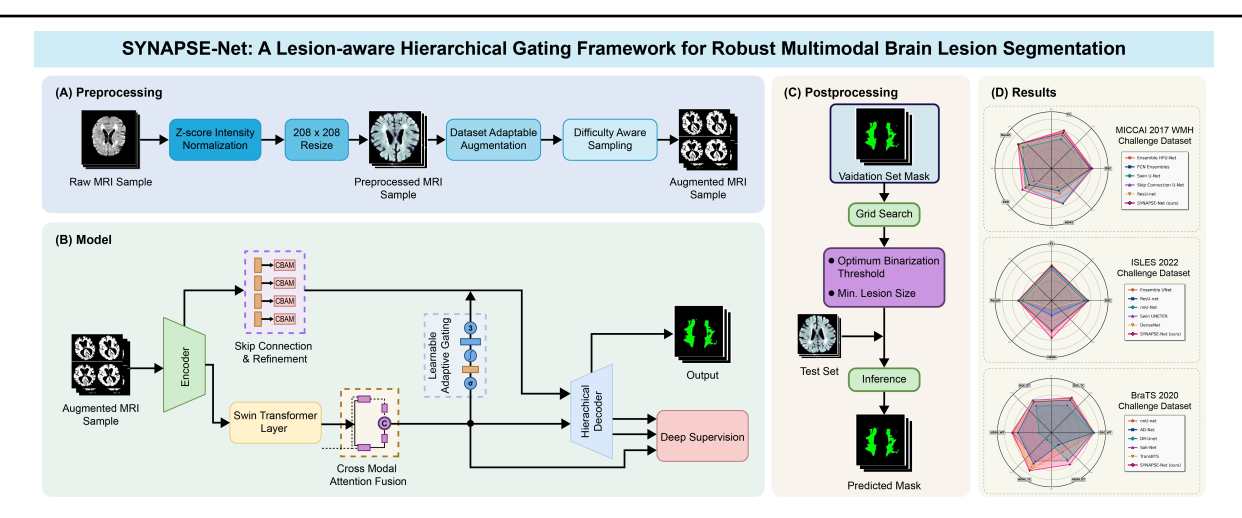
Automated segmentation of heterogeneous brain lesions from multi-modal MRI remains a critical challenge in clinical neuroima ing. Current deep learning models are typically specialized 'point solutions' that lack generalization and high performance va ance, limiting their clinical reliability. To address these gaps, we propose the Unified Multi-Stream SYNAPSE-Net, an adapti framework designed for both generalization and robustness. The framework is built on a novel hybrid architecture integrati multi-stream CNN encoders, a Swin Transformer bottleneck for global context, a dynamic cross-modal attention fusion (CMA mechanism, and a hierarchical gated decoder for high-fidelity mask reconstruction. The architecture is trained with a varian reduction strategy that combines pathology specific data augmentation and difficulty-aware sampling method. The model we evaluated on three different challenging public datasets: the MICCAI 2017 WMH Challenge, the ISLES 2022 Challenge, a the BraTS 2020 Challenge. Our framework attained a state-of-the-art DSC value of 0.831 with the HD95 value of 3.03 in the BraTS 2020, it reached the highest DSC value for the tumor core region (0.8651). These experimental findin suggest that our unified adaptive framework achieves state-of-the-art performance across multiple brain pathologies, providing robust and clinically feasible solution for automated segmentation. The source code and the pre-trained models are available https://github.com/mubid-01/SYNAPSE-Net-pre.

Keywords: Brain Lesion Segmentation; Unified Framework; Multi-modal Learning; Cross-Modal Attention; Lesion Condition

G R A P H I C A L A B S T R A C T

SYNAPSE-Net: A Lesion-aware Hierarchical Gating Framework for Robust Multimodal Brain Lesion Segmentation

(I) Results and I was a state-of-the-art performance across multiple brain pathologies, providing the proposed of the pr Automated segmentation of heterogeneous brain lesions from multi-modal MRI remains a critical challenge in clinical neuroimaging. Current deep learning models are typically specialized 'point solutions' that lack generalization and high performance variance, limiting their clinical reliability. To address these gaps, we propose the Unified Multi-Stream SYNAPSE-Net, an adaptive framework designed for both generalization and robustness. The framework is built on a novel hybrid architecture integrating multi-stream CNN encoders, a Swin Transformer bottleneck for global context, a dynamic cross-modal attention fusion (CMAF) mechanism, and a hierarchical gated decoder for high-fidelity mask reconstruction. The architecture is trained with a variance reduction strategy that combines pathology specific data augmentation and difficulty-aware sampling method. The model was evaluated on three different challenging public datasets: the MICCAI 2017 WMH Challenge, the ISLES 2022 Challenge, and the BraTS 2020 Challenge. Our framework attained a state-of-the-art DSC value of 0.831 with the HD95 value of 3.03 in the WMH dataset. For ISLES 2022, it achieved the best boundary accuracy with a statistically significant difference (HD95 value of 9.69). For BraTS 2020, it reached the highest DSC value for the tumor core region (0.8651). These experimental findings suggest that our unified adaptive framework achieves state-of-the-art performance across multiple brain pathologies, providing a robust and clinically feasible solution for automated segmentation. The source code and the pre-trained models are available at



1. Introduction

Quantitative analysis of brain lesions from magnetic resonance imaging (MRI) is fundamental to modern neurology, underpinning the diagnosis, prognosis, and therapeutic monitoring for a spectrum of disorders that includes cognitive decline, ischemic stroke, glioblastoma, and Alzheimer's disease (Barber et al., 1999; Capirossi et al., 2023; Grochans et al., 2022). White matter hyperintensities (WMHs), appear as hyperintense signals on FLAIR and T2-weighted imaging sequences, are an important primary radiological sign of small vessel disease of the brain and correlate significantly with cognitive impairment,

^{*}Corresponding author

¹Email: m.hassan.bme@gmail.com

dementia and stroke risk (Du et al., 2025). Acute as well as malignant and chronic diseases require intensive imaging evaluations. Multiforme glioblastoma, representing the most common type of primary brain malignancy, increasingly common worldwide and affects patient mortality substantially. It highlights the significant need for accurate delineation of the tumor for the purpose of surgical treatment and radiation therapy (Grochans et al., 2022; Johnson, 2012). Analogously, the diagnosis of ischemic stroke lesions must occur promptly and accurately within a time-limited window so as to provide optimal treatment intervention with the patient outcome improvement (Capirossi et al., 2023; Li et al., 2024; Liu et al., 2025). The characteristic WMH accumulation and cortical atrophy in Alzheimer's disease and dementias provide useful parameter for monitoring biomarkers (Barber et al., 1999; Sachdey, 2005).

The difficulty of the problem of manual segmentation is significant both clinically and in research applications due to its laboriousness and expense of large studies. Besides, the variability between different raters is high as well, which results in the inconsistency in measurement (Sachdev, 2005; Vanderbecq et al., 2020). These problems limit the growth of neuroimaging studies and the applicability of quantitative analysis in the field. Hence, the development of automated segmentation methods plays an important role for the field of neuroimaging studies. Recent advancements in deep learning show that algorithms can surpass the ability of expert human raters in segmenting brain lesions on different MRI protocols in different pathological conditions (Du et al., 2025; Duarte et al., 2024; Ronneberger et al., 2015).

Convolutional neural networks (CNNs) have advanced medical image analysis by automatically learning features from image datasets (Ronneberger et al., 2015; Demeusy et al., 2024). The U-Net architecture has become popular due to its encoderdecoder organization with skip connections that effectively handle contextual information while retaining spatial information to achieve accurate segmentation (Ronneberger et al., 2015; Punn and Agarwal, 2022; Azad et al., 2024). The success of the U-Net has led to specialized models to adapt for specific pathologies. U-Net variants including multi-scale extraction, attention mechanisms, and enhanced skip connections have been developed for better WMH segmentation which involves small lesions with indistinct edges (Wu et al., 2019; Park et al., 2021; He et al., 2025). U-Net and its variants were also finetuned for glioblastoma subregion segmentation challenges such as BraTS (Walsh et al., 2022; Zheng et al., 2022; R et al., 2025). For ischemic stroke, ensemble CNNs, hybrid architectures, and 3D residual networks improved acute lesion identification from diffusion-weighted imaging (DWI) (Tomita et al., 2020; Gheibi et al., 2023; Yassin et al., 2024). These targeted developments have yielded effective solutions for various neurodegenerative and pathological states (Chaki and Woźniak, 2023).

With the growth of the domain, studies increased beyond architectural fine-tuning to methodological frameworks. One of the major challenges to address was the missing annotations, which was then solved by the paradigms of semi-supervised and weakly supervised learning that utilized unlabeled or weakly labeled data to improve performance in data-scarce settings

(Duarte et al., 2024; Huang et al., 2023). At the same time, multi-center validation studies have demonstrated model robustness and generalizability across various datasets and machines (Gaubert et al., 2023; Namgung et al., 2025). Self-supervised learning approaches also improved model stability by enabling networks to learn features on unlabeled data (Wu et al., 2025; Zhang et al., 2023b; Tomasetti et al., 2023).

This methodological progress was matched by an architectural shift to overcome the inability of classic convolutional neural networks (CNNs) to capture long-range spatial interdependencies (Takahashi et al., 2024; Chen et al., 2024, 2025). Vision Transformers (ViTs) and Swin Transformers leverage self-attention mechanisms to model long-range spatial contexts (Hatamizadeh et al., 2022; Ayoub et al., 2023; Abbaoui et al., 2024). However, the most successful models have been hybrid architectures. For example, TransUNet and Swin-Unet use CNNs to capture local features and Transformers to process global context, and they excel on diverse brain pathologies (He et al., 2025; Chen et al., 2024; Hatamizadeh et al., 2022; Viteri et al., 2022). The breakthroughs were aided by multimodal fusion models that integrate information across diverse MRI sequences and by composite loss functions (Zhang et al., 2023a; Raju et al., 2024; Cabezas and Diez, 2024).

Despite significant technological progress, two major gaps hamper the clinical translation of automated segmentation tools. The first one is the lack of generalizability. Current studies often provide task-specific solutions, with models for WMH differing from those used for glioblastoma or ischemic stroke (Wu et al., 2023; Luo et al., 2024; de la Rosa et al., 2025). This restricts clinical application, since healthcare environments require versatile models rather than single-purpose systems demanding separate maintenance (Chau et al., 2025). The second and more critical gap is variance and reliability of performances. Most of the models act unpredictably, obtaining decent dice score but performing poorly with small or nonhomogenous cases, which are the circumstances that demand robust methods (He et al., 2025). This unpredictability undermines the clinical trust and hinders their application in critical cases.

To address these limitations, we introduce SYNAPSE-Net, a novel hybrid CNN-Transformer framework designed for effective and robust segmentation of heterogeneous brain lesions across multi-modal MRI. This study contains a single, multi-stream model of fixed architecture, tuned for three clinical applications: WMH, ischemic stroke, and glioblastoma segmentation. Experimental results on three publicly available datasets demonstrate our algorithm to attain state-of-the-art accuracy and higher generalizability and robustness over specialized models. The key contributions of our work include:

- We propose a single, unified deep learning framework and validate its capability to achieve robust and accurate segmentation across clinically distinct and heterogeneous brain pathologies. To our knowledge, this is the first demonstration of a single, fixed architecture achieving state-of-the-art performance across such diverse tasks.
- We introduce a novel hybrid architecture that synergisti-

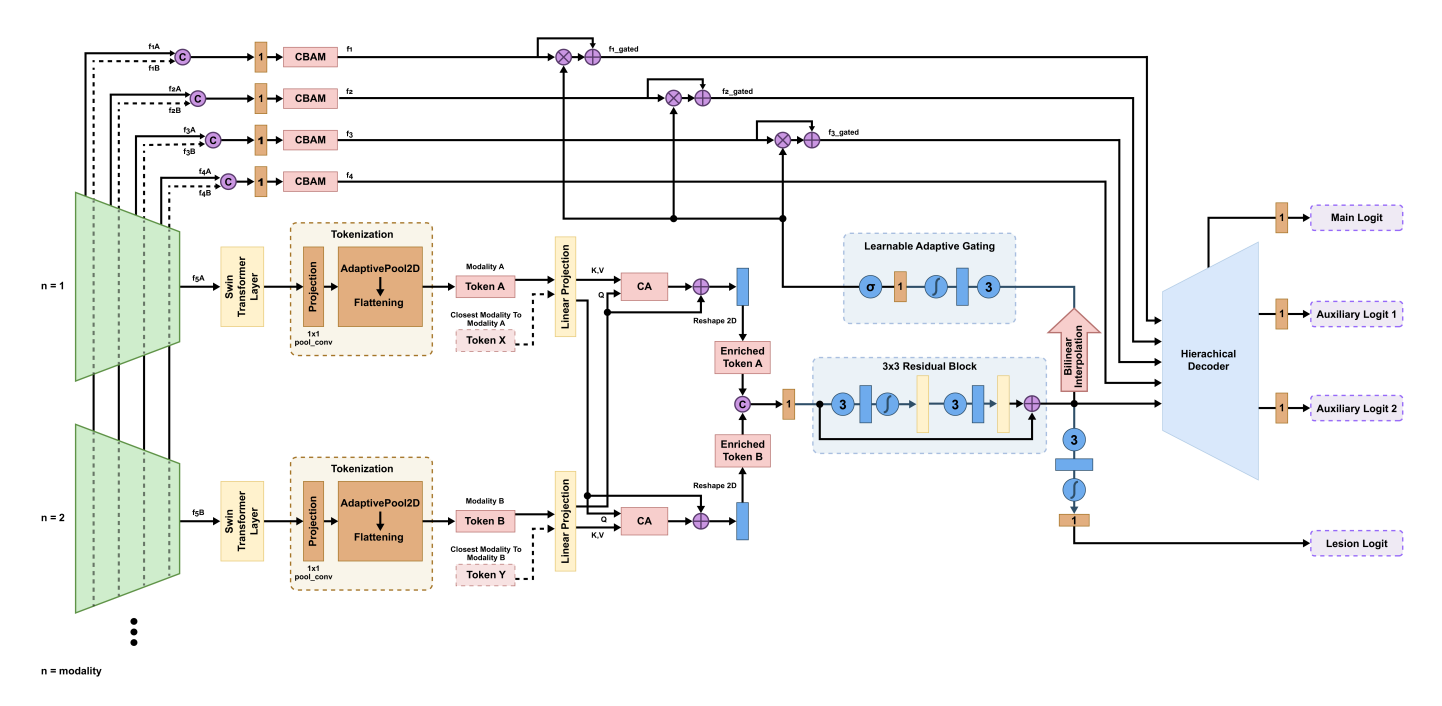


Figure 1: The SYNAPSE-Net architecture, consisting of N parallel CNN encoders, a hybrid bottleneck that fuses modalities using Swin Transformers and Cross-Modal Attention, and a Hierarchical Gated Decoder with a UNet++ backbone to generate the final segmentation.

cally integrates multi-stream CNNs for specialized local feature extraction, a Swin Transformer for global contextual modeling, and a cross-modal attention mechanism for intelligent, adaptive multi-modal fusion.

- We present an adaptive variance-reduction training strategy that combines data-driven difficulty-aware sampling with a pathology-specific composite loss function, which is shown to explicitly minimize performance inconsistency and improve reliability on clinically challenging cases.
- Our framework is rigorously validated on three public benchmark datasets, where it is shown to outperform numerous leading, specialized models, demonstrating the superior generalization and robustness of our unified approach and highlighting its potential for clinical translation.

The multi-stream encoder enables the model to learn the adaptation process for multi-modal inputs per pathology. The Swin Transformer bottleneck improves the receptive field and uses global context for precise large lesion segmentation. The CMAF mechanism enables more advanced information fusion than simple concatenation, leading to improved segmentation outcomes. Further, the hierarchical gated decoder improves accuracy by using higher-level features to regulate the reconstruction process, suppressing noise and concentrating on significant areas. Finally, the adaptive variance-reduction training approach addresses performance inconsistency. The difficulty-aware sampling helps the model to learn the small, subtle lesions where the model is most likely to miss out. The pathology-specific composite loss function provides a concentrated learning signal for counterbalancing the most significant

sources of error for varied tasks and ensures satisfactory recall and high spatial accuracy at the same time.

The remainder of this paper is organized as follows: Section 2 details our proposed methodology, including the model architecture and training strategy. Section 3 presents a comprehensive details of experimental setup, utilities of different parts of our proposed framework through ablation studies and results across the three target pathologies. Section 4 offers our limitations and future directions, and section 5 provides our short discussion of the results, followed by our concluding remarks.

2. Methodology

2.1. Framework Overview

Our methodology is centered on a unified multi-stream, endto-end deep learning model for segmenting diverse brain lesions in multi-modal MRI images. The model utilizes a constant architectural blueprint that adaptively configures to the number and types of modalities required for a specific clinical task. This allows it to handle a range of pathologies, from dual-modality dataset like WMH and ISLES to quad-modality dataset such as BraTS, addressing the need for effective generalization. As shown in Fig. 1, the SYNAPSE-Net data flow consists of three synergistic phases. First, a multi-stream feature encoding phase uses parallel CNN encoders for independent, modality-specific feature extraction, preserving crucial pathological signals. Shallow and intermediate features are then fused for unified skip connections to the decoder. Second, a hybrid bottleneck enriches the deep features from each encoder by incorporating global context with Swin Transformer layers, followed by an adaptive cross-modal attention fusion (CMAF) mechanism for collective integration. Third, this bottleneck representation is passed to a hierarchical, lesion-aware gated decoder with a UNet++ structure, which employs top-down attention gating and deep supervision to generate accurate segmentation masks. The following subsections will detail these phases.

2.2. Multi-Stream Feature Encoding and Skip Connection Refinement

The first stage of SYNAPSE-Net learns hierarchical features from each of the N input MRI modalities. To preserve modality-specific information, each sequence is processed through an independent, architecturally identical CNN encoder before any feature fusion occurs. This late-fusion approach prevents the loss of subtle but crucial pathological indicators unique to certain modalities, such as the diffusion patterns in DWI or contrast enhancement characteristics in T1c images.

Each encoder instantiates a five-stage network designed for incremental feature abstraction as depicted in Fig. 2. The methodology systematically reduces spatial resolution using max-pooling as it concurrently increases channel depth to extract increasingly complex and semantically abstract features. This approach yields two distinct sets of outputs per modality stream m: a set of multi-scale feature maps suitable for skip connections, $\{\mathbf{f}_{i,m}|i\in\{1,2,3,4\}\}$, that maintain high-resolution spatial information, as well as a low resolution feature map $\mathbf{f}_{5,m}$ that captures the highest abstract semantic context and is then passed on towards the hybrid bottleneck.

Before being used in the decoder, the modality-specific skip connections from all N streams are adaptively refined and fused at each resolution level, i. A unified and semantically rich representation of the multi-modal inputs is provided to the decoder by this preliminary fusion. The process involves concatenating the feature maps across all streams, $\mathbf{f}_{i,\text{cat}} = [\mathbf{f}_{i,1}; \dots; \mathbf{f}_{i,N}]$. A subsequent 1×1 convolution, with learnable weights \mathbf{W}_{proj} , then projects this tensor back to the original channel dimension, c_i :

$$\mathbf{f}_{i,\text{proj}} = \mathbf{W}_{\text{proj}} * \mathbf{f}_{i,\text{cat}} \tag{1}$$

where (*) denotes the convolution operation. This learnable projection allows the model to prioritize the most informative modalities at each feature scale by adaptively weighing their contributions.

The target feature map is then processed by CBAM (Woo et al., 2018) that enables widespread feature enhancement. CBAM constitutes a condensed and dynamic module that successively obtains attention maps along channel and spatial axes. The entire process that can be applied on an intermediate feature map ${\bf F}$ can be formulated as below:

$$\mathbf{F}' = \mathbf{M}_c(\mathbf{F}) \odot \mathbf{F} \tag{2}$$

$$\mathbf{F}'' = \mathbf{M}_s(\mathbf{F}') \odot \mathbf{F}' \tag{3}$$

where \odot is element-wise product, and \mathbf{M}_c and \mathbf{M}_s are the channel and spatial attention maps, respectively. The channel attention module first aggregates spatial information by using both

average pooling and max pooling layers that feed into a common multi-layer perceptron (MLP) for calculating the channel attention map \mathbf{M}_c :

$$\mathbf{M}_{c}(\mathbf{F}) = \sigma(\mathrm{MLP}(\mathrm{AvgPool}(\mathbf{F})) + \mathrm{MLP}(\mathrm{MaxPool}(\mathbf{F})))$$
 (4)

The spatial attention module pools channel information into two 2D maps that get concatenated and convolved by a 7×7 layer in order to create the spatial attention map \mathbf{M}_s :

$$\mathbf{M}_{s}(\mathbf{F}') = \sigma(f^{7 \times 7}([\operatorname{AvgPool}(\mathbf{F}'); \operatorname{MaxPool}(\mathbf{F}')]))$$
 (5)

where σ is the sigmoid function. The final output of this stage is a set of pre-fused, attention-refined skip connections, $\{\mathbf{f}_i|i\in\{1,2,3,4\}\}$, which are passed to the hierarchical gated decoder.

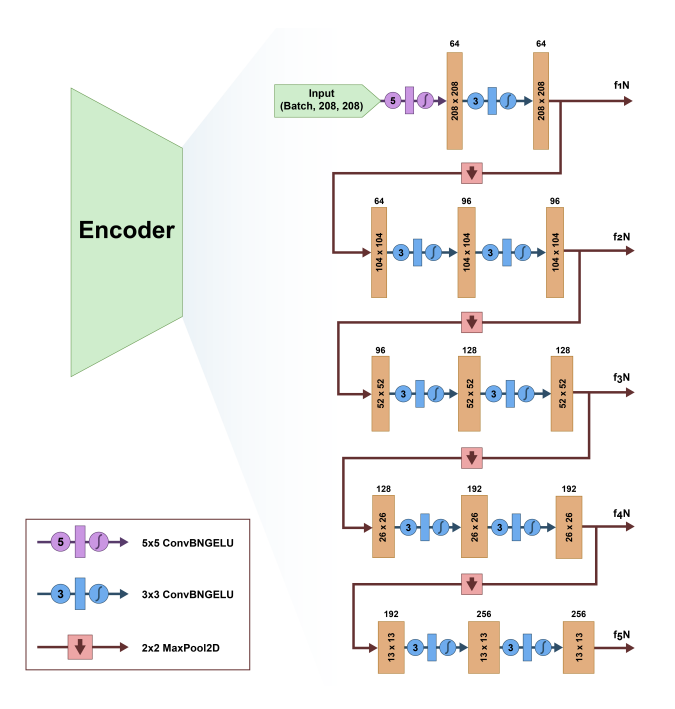


Figure 2: The five-stage Encoder for extracting five levels of feature maps $(f_1$ to $f_5)$ for each input modality.

2.3. Hybrid Bottleneck: Global Context and Cross-Modal Fusion

In this stage, the deepest feature maps from each stream, $\{\mathbf{f}_{5,m}\}$, enter the hybrid bottleneck after encoding to overcome the limited receptive fields of CNNs to create semantically-rich feature representation. The process involves two primary steps: first, Swin Transformers (Liu et al., 2021) are applied for intramodality refinement to capture global context. Subsequently, an adaptive fusion block employs cross-modal attention to efficiently merge the features from all streams, producing a unified bottleneck representation.

2.3.1. Intra-Modal Refinement with Swin Transformers

At first, every deep feature map $\mathbf{f}_{5,m}$ is independently passed through Swin Transformer layers. It enriches the local, translation-equivariant features extracted by the CNN with

deep, global spatial context for each modality individually, before any fusion is applied. The core of Swin Transformer is the multi-head self-attention (MSA) mechanism which is defined below:

Attention(Q, K, V) = Softmax
$$\left(\frac{QK^T}{\sqrt{d_k}} + B\right)V$$
 (6)

here **Q**, **K**, **V** are the query, key, and value matrices derived from the same input tensor, and **B** is a learnable relative position bias. A Swin Transformer layer is composed of two successive Swin-T blocks. The computation for a consecutive pair of blocks for a layer *l* is formulated as:

$$\hat{\mathbf{z}}^{l} = \text{W-MSA}(\text{LN}(\mathbf{z}^{l-1})) + \mathbf{z}^{l-1}$$
(7)

$$\mathbf{z}^{l} = \text{MLP}(\text{LN}(\mathbf{\hat{z}}^{l})) + \mathbf{\hat{z}}^{l}$$
(8)

$$\hat{\mathbf{z}}^{l+1} = \text{SW-MSA}(\text{LN}(\mathbf{z}^l)) + \mathbf{z}^l$$
 (9)

$$\mathbf{z}^{l+1} = \text{MLP}(\text{LN}(\hat{\mathbf{z}}^{l+1})) + \hat{\mathbf{z}}^{l+1}$$
(10)

where W-MSA and SW-MSA denote Windowed and Shifted-Window MSA, respectively, and \mathbf{z}^l is the output of the MLP for block l. The W-MSA module computes self-attention over local non-overlapping windows, while the SW-MSA module shifts the arrangement of windows spatially to allow cross-window computation.

2.3.2. Adaptive Cross-Modal Attention Fusion (CMAF)

The central module for context-enriched features fusion is the CMAF bottleneck (Sun et al., 2024), designed to enable different modality streams to mutually query and enrich one another. The mechanism employs a priority-based pairing strategy to handle variable input modalities robustly, as formalized in Algorithm 1.

First, feature maps are tokenized into sequences $\{T_m|m\in\{1,\ldots,N\}\}$. The pairing strategy prepares inputs for bidirectional cross-attention by grouping modalities into natural pairs based on physical contrast principles: T1w contrast, T2w contrast, and proton weighted contrast. If the remainder is an unpaired stream, it serves as "universal context" and is concatenated to both primary streams before fusion that ensures comprehensive information integration.

The resulting vectors \mathbf{T}_A and \mathbf{T}_B are processed using bidirectional multi-head cross-attention (Ates et al., 2023):

$$CrossAtt(\mathbf{Q}_A, \mathbf{K}_B, \mathbf{V}_B) = Attention(\mathbf{Q}_A, \mathbf{K}_B, \mathbf{V}_B)$$
 (11)

The reciprocal operation is performed concurrently. The outputs are added back to their original input tokens via a residual connection and normalized to produce two enriched token sequences, \mathbf{T}'_A and \mathbf{T}'_B :

$$\mathbf{T}_{A}' = \mathrm{LN}(\mathbf{T}_{A} + \mathrm{CrossAtt}(\mathbf{Q}_{A}, \mathbf{K}_{B}, \mathbf{V}_{B})) \tag{12}$$

$$\mathbf{T}_{B}' = LN(\mathbf{T}_{B} + CrossAtt(\mathbf{Q}_{B}, \mathbf{K}_{A}, \mathbf{V}_{A}))$$
 (13)

Lastly, the enriched tokens get de-tokenized back into a spatial grid, concatenated, projected through a 1×1 convolution, and fed through a final residual block. The end-result of this procedure is the final bottleneck tensor which acts as the rich semantic base for the decoder.

```
Algorithm 1: Priority-Based Pairing and Fusion Strategy
```

% N token streams

Input: $\{T_1, ..., T_N\}$;

```
Output: T'_A, T'_B;
                                                                   % Enriched tokens
  1 \mathcal{P} \leftarrow \emptyset; \mathcal{T} \leftarrow \{T_1, \ldots, T_N\};
     % Form natural modality pairs
 2 foreach
        (a,b) \in \{(T1w,T1c),(FLAIR,T2w),(DWI,ADC)\}\ do
            if T_a, T_b \in \mathcal{T} then
                 \mathcal{P} \leftarrow \mathcal{P} \cup \{[T_a; T_b]\}; \mathcal{T} \leftarrow \mathcal{T} \setminus \{T_a, T_b\}
 5 O \leftarrow \mathcal{T}:
 6 if |\mathcal{P}| = 2 then
            T_A \leftarrow \mathcal{P}[0]; T_B \leftarrow \mathcal{P}[1]
 8 else if |\mathcal{P}| = 1 and |O| = 1 then
           T_A \leftarrow \mathcal{P}[0]; T_B \leftarrow \mathcal{O}[0]
10 else if |\mathcal{P}| = 1 and |\mathcal{O}| = 2 then
            T_A \leftarrow \mathcal{P}[0]; T_B \leftarrow O[0]; T_{\text{ctx}} \leftarrow O[1];
              T_A \leftarrow [T_A; T_{\text{ctx}}]; T_B \leftarrow [T_B; T_{\text{ctx}}]
12 else
            T_A \leftarrow \text{Concat}(\mathcal{P} \cup \mathcal{O}[0 : \lfloor |\mathcal{O}|/2 \rfloor]);
         T_B \leftarrow \operatorname{Concat}(O[\lfloor |O|/2 \rfloor :]) 
14 T'_A, T'_B \leftarrow \text{FusionBottleneck}(T_A, T_B);
15 return T'_A, T'_B;
```

2.4. Hierarchical Gated Decoder

The last component of the SYNAPSE-Net is the nested decoder specially designed for the exact reconstruction of the high fidelity segmentation mask. Here, basic UNet++ architecture (Zhou et al., 2018) is improved by the incorporation of our hierarchical adaptive gating mechanism. This novel structure reconstructs the mask by focusing on the rich pathological context derived from the network's deep feature bottleneck by creating an iterative series of progressively detailed attention. The conceptual data flow is depicted in Fig. 3, and the detailed practical outline is in Fig. 4.

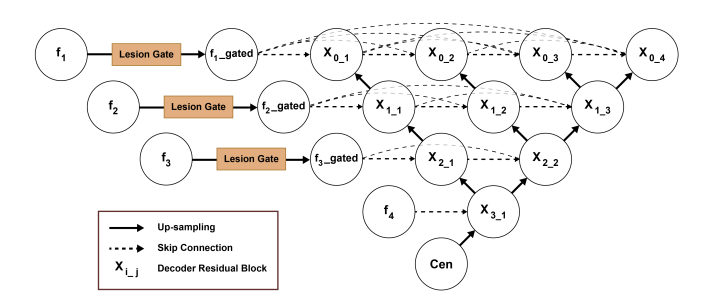


Figure 3: Conceptual diagram of the Hierarchical Gated Decoder, where Lesion Gate modules refine skip connections (f_1-f_4) before feeding them into the dense UNet++ decoder nodes $(X_{i,j})$.

2.4.1. The Hierarchical Adaptive Gating Mechanism

Before entering the decoder backbone, pre-fused skip connections (\mathbf{f}_i) first undergo hierarchical gating refinement. It implements top-down feature modulation by a set of 'Lesion

Gate' modules. A module utilizes a skip connection along with a guidance signal (g) from a more semantically abstract layer to compute a spatial attention gate, S_{gate} :

$$\mathbf{S}_{\text{gate}} = C(\mathcal{U}(\mathbf{g})) \tag{14}$$

where C is a small convolutional block and $\mathcal{U}(\cdot)$ is an upsampling operation. This gate then additively refines the original skip connection features via a residual connection for stable training:

$$\mathbf{f}_{i,\text{gated}} = \mathbf{f}_i + \left(\mathbf{f}_i \odot \sigma(\mathbf{S}_{\text{gate}})\right) \tag{15}$$

where σ is the sigmoid activation and \odot denotes element-wise multiplication.

This creates a chain of attention that starts with the abstract characteristics and increasingly focusing on features of high resolution:

$$\mathbf{f}_{3,\text{gated}} = \text{LesionGate}(\mathbf{f}_3, \mathbf{center})$$
 (16)

$$\mathbf{f}_{2,\text{gated}} = \text{LesionGate}(\mathbf{f}_2, \mathbf{x}_{3,1})$$
 (17)

$$\mathbf{f}_{1,\text{gated}} = \text{LesionGate}(\mathbf{f}_1, \mathbf{x}_{2,2})$$
 (18)

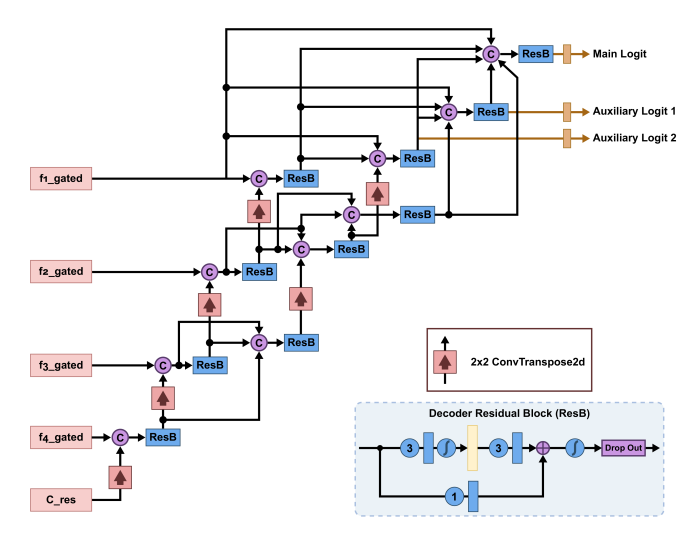


Figure 4: The hierarchical gated decoder realization using the dense UNet++ backbone, where the gated skip connections ($f_{i,gated}$) and bottleneck tensor are utilized.

2.4.2. UNet++ Decoder Backbone

The decoder network is based on the UNet++ architecture, where nested dense skip paths effectively bridge the semantic gap between encoder and decoder features. Let $\mathbf{x}_{i,j}$ be a decoder node's output, where 'i' represents the down-sampling level, 'j' specifies the convolutional layer in the dense skip pathway and $\mathcal{H}(\cdot)$ as the operation which is defined as residual block. The flow of information starts at the bottom level where the first computation node, $\mathbf{x}_{3,1}$, occurs by fusing the up-sampled center tensor exiting the bottleneck with the \mathbf{f}_4 skip connection:

$$\mathbf{x}_{3,1} = \mathcal{H}([\mathbf{f}_4, \mathcal{U}(\mathbf{center})]) \tag{19}$$

Each first node in a shallower pathway is computed by combining the up-sampled output from the lower node with the corresponding gated skip connection, The consecutive mathematical equations are given as:

$$\mathbf{x}_{2,1} = \mathcal{H}([\mathbf{f}_{3,\text{gated}}, \mathcal{U}(\mathbf{x}_{3,1})]) \tag{20}$$

$$\mathbf{x}_{1,1} = \mathcal{H}([\mathbf{f}_{2,\text{gated}}, \mathcal{U}(\mathbf{x}_{2,1})]) \tag{21}$$

$$\mathbf{x}_{0,1} = \mathcal{H}([\mathbf{f}_{1,\text{gated}}, \mathcal{U}(\mathbf{x}_{1,1})]) \tag{22}$$

In every row, the subsequent nodes (j > 1) are determined as the integral concatenation of all the prior feature maps of the respective row by the up-sampled nodal output according to the standard UNet++ configuration:

$$\mathbf{x}_{i,j} = \mathcal{H}\left(\left[\left\{\mathbf{x}_{i,k}\right\}_{k=0}^{j-1}, \mathcal{U}(\mathbf{x}_{i+1,j-1})\right]\right)$$
(23)

This hierarchical structure allows the model to produce highly accurate and detailed segmentation masks.

2.4.3. Deep Supervision and Final Output Generation

The architectural structure implements a deep supervision mechanism by generating multiple outputs to allow a vast gradient flow. The last row consisting of decoder nodes, i.e., $\mathbf{x}_{0,2}$, $\mathbf{x}_{0,3}$, and $\mathbf{x}_{0,4}$, that correspond to segmentations obtained by implicit U-Nets with varied depths, each passes through a terminating 1×1 convolutional head to give two auxiliary logit maps $(\mathbf{z}_{\text{aux},1},\mathbf{z}_{\text{aux},2})$ and the main logit map $(\mathbf{z}_{\text{main}})$. Additionally, auxiliary head is attached directly to the 'center' tensor to produce a low-resolution lesion localization map, $\mathbf{z}_{\text{lesion}}$. In training, supervision is enforced on these auxiliary logits and only the main logit from the deepest path $(\mathbf{x}_{0,4})$ is used for inference.

2.5. Model Loss Function

The training of the framework is guided by an adaptive, composite loss function, \mathcal{L}_{total} . It is a weighted sum of a main loss (\mathcal{L}_{main}), an auxiliary deep supervision loss (\mathcal{L}_{aux}), and a bottleneck lesion localization loss (\mathcal{L}_{lesion}).

$$\mathcal{L}_{\text{total}} = \mathcal{L}_{\text{main}} + \mathcal{L}_{\text{aux}} + \lambda_{\text{lesion}} \mathcal{L}_{\text{lesion}}$$
 (24)

2.5.1. Foundational Loss Functions

Dice and Focal Loss: The Dice Loss maximizes overlap between predictions P and ground truth T.

$$\mathcal{L}_{\text{Dice}}(P, T) = 1 - \frac{2\sum_{i=1}^{N} P_i T_i + \epsilon}{\sum_{i=1}^{N} P_i + \sum_{i=1}^{N} T_i + \epsilon}$$
(25)

where ϵ is a smoothing constant. Focal Loss addresses class imbalance by scaling the cross-entropy loss by $(1 - p_t)^{\gamma}$.

$$\mathcal{L}_{\text{Focal}}(p, y) = -\alpha_t (1 - p_t)^{\gamma} \log(p_t)$$
 (26)

where p_t is the probability of the correct class, and γ and α_t are focusing and balancing parameters.

Tversky and Boundary Loss: The Tversky Loss generalizes the Dice loss to control the trade-off between false positives

Table 1: Pathology-Adapted Data Augmentation Protocols

Dataset	Random Flips	Affine Probability	Rotation Range	Scale Range	Elastic Deformation	Photometric Augmentation	Channel Dropout
WMH (Highest)	50%	75%	±20°	±20%	50%	30-50%	50%
ISLES (Medium)	50%	75%	±15°	±15%	30%	30%	25%
BraTS (Lowest)	50%	50%	±10°	±10%	-	15-20%	-

Note: The intensity of on-the-fly transforms was tiered from highest (WMH) to lowest (BraTS) to match the specific characteristics of each pathology and dataset size. Dash (-) indicates the augmentation was not applied.

(FP) and false negatives (FN) via parameters α and β .

$$\mathcal{L}_{\text{Tversky}}(P, T; \alpha, \beta) = 1 - \frac{\sum_{i} P_{i} T_{i} + \epsilon}{\sum_{i} P_{i} T_{i} + \alpha \sum_{i} P_{i} (1 - T_{i}) + \beta \sum_{i} (1 - P_{i}) T_{i} + \epsilon}$$
(27)

Setting $\beta > \alpha$ penalizes FNs more heavily. We merge Focal and Tversky losses into a weighted sum, $\mathcal{L}_{FocalTversky}$.

$$\mathcal{L}_{\text{FocalTversky}} = w_f \mathcal{L}_{\text{Focal}} + w_t \mathcal{L}_{\text{Tversky}}$$
 (28)

To improve geometric accuracy, a Boundary Loss (Kervadec et al., 2018) penalizes predictions far from the ground truth boundary using a pre-computed Euclidean distance map d_G .

$$\mathcal{L}_{\text{Boundary}}(P, d_G) = \frac{1}{N} \sum_{i=1}^{N} P_i \cdot (d_G)_i$$
 (29)

2.5.2. Pathology-Specific Loss Configurations

We adapt the total loss for each pathology. In our formulations, z_{main} , $z_{\text{aux},k}$, and z_{lesion} are the raw logit outputs from the main, k-th auxiliary, and bottleneck heads, respectively. The ground-truth mask is y, $\sigma(\cdot)$ is the sigmoid function, and \downarrow is a downsampling operator.

Vascular Lesion Loss (WMH & ISLES):

$$\mathcal{L}_{\text{main}}^{\text{Vascular}} = \mathcal{L}_{\text{FocalTversky}}(z_{\text{main}}, y) + \lambda_b \mathcal{L}_{\text{Boundary}}(\sigma(z_{\text{main}}), y)$$

(30)

$$\mathcal{L}_{\text{aux}}^{\text{Vascular}} = \sum_{k} w_k \cdot \mathcal{L}_{\text{FocalTversky}}(z_{\text{aux},k}, y)$$
 (31)

$$\mathcal{L}_{lesion} = \mathcal{L}_{Focal}(z_{lesion}, \downarrow y)$$
(32)

Brain Tumor Loss (BraTS):

$$\mathcal{L}_{\text{main}}^{\text{BraTS}} = \mathcal{L}_{\text{Dice}}(z_{\text{main}}, y) \tag{33}$$

$$\mathcal{L}_{\text{main}}^{\text{BraTS}} = \mathcal{L}_{\text{Dice}}(z_{\text{main}}, y)$$

$$\mathcal{L}_{\text{aux}}^{\text{BraTS}} = \sum_{k} w_k \cdot \mathcal{L}_{\text{Dice}}(z_{\text{aux},k}, y)$$
(33)

$$\mathcal{L}_{lesion} = \mathcal{L}_{Focal}(z_{lesion}, \downarrow y_{lesion})$$
 (35)

Here, the lesion target y_{lesion} is a binary mask of the entire tumor region, derived from the multi-class ground truth via an indicator function, $y_{\text{lesion}} = (\mathbf{1}_{y>0})$.

3. Experimental Results

3.1. Datasets

Our framework's performance was evaluated on three distinct, publicly available benchmark datasets^{2,3,4} each chosen for its unique and difficult segmentation challenge. For vascular lesion segmentation, two multi-center datasets were utilized. The first, for chronic small vessel disease, is the MICCAI 2017 White Matter Hyperintensities (WMH) Challenge dataset (Kuijf et al., 2022). It has a training set of 60 subjects, acquired across three hospitals on five different 1.5T and 3T scanner models, was split into 48 for training and 12 for validation, while the test set comprises 110 subjects. We utilized the provided 3D T1-weighted (T1w) and T2 FLAIR sequences, with ground truth provided as expert manual annotations of WMH.

The second vascular dataset, for acute stroke, is the Ischemic Stroke Lesion Segmentation (ISLES) 2022 Challenge dataset (Hernandez Petzsche et al., 2022). This dataset provides 250 training cases from three multi-vendor stroke centers, which we partitioned into 200 for training and 50 for validation, while the official test data of 150 hidden cases were used for final ranking by the challenge organizers. For this task, the DWI and ADC map sequences were utilized, with ground truth provided as expert-revised segmentations of the ischemic lesion core.

For segmenting heterogenous pre-operative brain tumors, we utilized the BraTS 2020 Challenge dataset (Menze et al., 2015; Bakas et al., 2017, 2018). The official training dataset consists of multi-parametric MRI scans from 660 diffuse glioma patients where training cohort contains 369 subjects, validation cohort has 125 subjects, while the final test was performed on a cohort of 166 cases. All four standard co-registered modalities were used: T1w, post-contrast T1c, T2w, and FLAIR. The ground truth consists of expert manual annotations for three nested, clinically relevant sub-regions given as the enhancing tumor (ET), the tumor core (TC), and the whole tumor (WT). This large, pre-operative dataset serves as a rigorous benchmark for evaluating performance on heterogeneous gliomas.

3.2. Implementation Details

A standardized preprocessing pipeline was applied across all datasets. Initial structural alignment was performed datasetspecifically: for the WMH Challenge dataset, we applied FSL's Brain Extraction Tool (BET) (Jenkinson et al., 2012) for

²https://doi.org/10.34894/AECRSD

³https://zenodo.org/records/7960856

⁴https://www.med.upenn.edu/cbica/brats2020/

skull stripping, while for ISLES 2022, we conducted rigid coregistration of the provided skull-stripped ADC and DWI volumes. The BraTS 2020 dataset came fully pre-processed from the organizers. Following alignment, a consistent Z-score intensity normalization was applied to all data, with statistics derived from the 2nd to 98th percentile of brain tissue intensities from the training subjects of each respective dataset. Finally, all axial slices were cropped or zero-padded to a uniform 208 × 208 matrix to serve as the 2D network input. To mitigate overfitting, we employed an adaptive, on-the-fly data augmentation strategy wherein the intensity of the augmentation protocol was specifically tailored to each pathology, as detailed in Table 1. For the vascular tasks, we enhanced robustness on small lesions by employing a difficulty-aware sampling strategy in the WMH and ISLES datasets. This method oversampled 2D slices containing lesions smaller than a pre-calculated volume percentile, forcing the model to focus on the most challenging cases. The hyperparameters for each training configuration, including the initial learning rate, total epochs, and optimizer details, are summarized in Table 2. All models were implemented in PyTorch and trained on a workspace with an NVIDIA Quadro RTX 5000 16GB GPU and an Intel Xenon® W-2265 3.50 GHz processor.

3.3. Inference Protocol and Post-processing

To ensure fair and reproducible evaluation across all clinical tasks, we implemented a rigorous two-step inference protocol (Algorithm 2) that systematically separates model inference from post-processing parameter selection. By preventing any information leakage from the test set during hyperparameter optimization, this approach guarantees an unbiased assessment. Hyperparameter tuning stage only uses the validation dataset. For each 3D validation case, we generate continuous probability volumes by means of sliding-window inference with a Gaussian weight function. This technique creates smooth 3D probability maps with no artifacts by analyzing axial slices with significant overlap and averaging the predictions in those regions.

We run a comprehensive grid search for the binarization threshold $\tau \in [0.10, 0.80]$ and minimum lesion size $S_{\min} \in \{2, 3, ..., 15\}$ voxels. The optimal parameters are selected to maximize the mean DSC across the validation cohort:

$$(\tau_{\rm opt}, S_{\rm min, opt}) = \underset{\tau, S_{\rm min}}{\arg \max} \mathbb{E}[\mathrm{DSC}(\hat{\mathbf{Y}}_{\rm val}, \mathbf{Y}_{\rm val})]$$
 (36)

The evaluation stage uses the computed optimal parameters $(\tau_{\rm opt}, S_{\rm min, opt})$ to the unseen test set. Sliding window predic-

Table 2: Network Training Parameters

	WMH	ISLES	BraTS
Learning Rate	1e-4	1e-4	5e-5
Epochs	150	120	300
Batch Size	18	18	8
Weight Decay	1.5e-4	1.5e-4	1e-4
Optimizer		AdamW	
LR Scheduler*	✓(15-epoch warmup + cos	sine)
5-Fold CV	✓	· /	X
Test-Time Aug.	✓	✓	Х

^{*} Linear warmup followed by cosine annealing decay.

Algorithm 2: Inference and Hyperparameter Tuning Protocol

% Trained model

Input: M;

```
1 \mathcal{D}_{val} = \{\mathbf{X}_{val}, \mathbf{Y}_{val}\};
                                                                             % Validation set
 2 \mathcal{D}_{\text{test}} = \{\mathbf{X}_{\text{test}}, \mathbf{Y}_{\text{test}}\};
                                                                                             % Test set
     Output: \mathcal{R}_{\text{metrics}};
                                                   % Final evaluation metrics
                                                                     % Optimal threshold
 3 	au_{\mathrm{opt}};
                                           % Optimal minimum lesion size
 4 S_{\text{min,opt}};
     % Stage 1: Hyperparameter Tuning on
           Validation Set
 5 \mathcal{P}_{\text{val}} \leftarrow F_{\text{inference}}(\mathbf{X}_{\text{val}}, \mathcal{M});
 6 \tau_{\text{opt}} \leftarrow 0.5; S_{\text{min,opt}} \leftarrow 0; S_{\text{best}} \leftarrow 0;
 7 for \tau \in [0.10, 0.80] do
             for S_{min} \in \{2, 3, ..., 15\} do
 8
                     \mathcal{L}_{\text{scores}} \leftarrow \emptyset;
 9
                     foreach (\mathbf{P}_i, \mathbf{Y}_i) \in (\mathcal{P}_{val}, \mathbf{Y}_{val}) do
10
                             \hat{\mathbf{Y}}_i \leftarrow F_{\text{postprocess}}(F_{\text{binarize}}(\mathbf{P}_i, \tau), S_{\text{min}});
11
                            s_i \leftarrow F_{\text{DSC}}(\hat{\mathbf{Y}}_i, \mathbf{Y}_i);
12
                         \mathcal{L}_{\text{scores}} \leftarrow \mathcal{L}_{\text{scores}} \cup \{s_i\};
13
                     \bar{s} \leftarrow F_{\text{mean}}(\mathcal{L}_{\text{scores}});
14
                     if \bar{s} > S_{best} then
15
                       % Stage 2: Final Evaluation on Test Set
17 \mathcal{R}_{\text{metrics}} \leftarrow \emptyset;
18 foreach (\mathbf{X}_i, \mathbf{Y}_i) \in \mathcal{D}_{test} do
             \mathbf{P}_j \leftarrow F_{\text{inference}}(\mathbf{X}_j, \mathcal{M});
             \hat{\mathbf{Y}}_j \leftarrow F_{\text{postprocess}}(F_{\text{binarize}}(\mathbf{P}_j, \tau_{\text{opt}}), S_{\text{min,opt}});
20
             \mathcal{M}_j \leftarrow F_{\text{calculate\_metrics}}(\hat{\mathbf{Y}}_j, \mathbf{Y}_j);
             \mathcal{R}_{\text{metrics}} \leftarrow \mathcal{R}_{\text{metrics}} \cup \{\mathcal{M}_i\};
23 return \mathcal{R}_{metrics}, \tau_{opt}, S_{min,opt};
```

tions over each test instance produce probability maps, which are then binarized at $\tau_{\rm opt}$ and processed with 3D connected-component analysis to filter out false positive predictions with area smaller than $S_{\rm min,opt}$. All metrics in our evaluation are derived from the final refined binary segmentations.

3.4. Evaluation Metrics

We evaluated model performance using voxel-level and object-level metrics. Also, to assess variability, the mean and standard deviation $(\pm SD)$ for all key metrics are reported.

3.4.1. Voxel-Level Metrics

Voxel-level metrics quantify segmentation accuracy by comparing each individual voxel in the predicted mask (\hat{Y}) and the ground truth (Y). The Dice Similarity Coefficient (DSC) is our primary metric for evaluating volumetric overlap:

$$DSC(Y, \hat{Y}) = \frac{2 \cdot |Y \cap \hat{Y}|}{|Y| + |\hat{Y}|} = \frac{2 \cdot TP}{2 \cdot TP + FP + FN}$$
(37)

The 95th Percentile Hausdorff Distance (HD95) measures boundary accuracy. At the same time, it is robust to outliers,

Table 3: Ablation Study of Training Pipeline Components on WMH Dataset

Training Protocol	DSC ↑	Lesion F1 ↑	Recall ↑	HD95 ↓	AVD ↓
Minimal Pipeline	0.765 ± 0.168	0.66 ± 0.211	0.68 ± 0.224	7.95 ± 5.81	31.54 ± 25.98
2. + Robust Preprocessing	0.791 ± 0.145	0.71 ± 0.185	0.72 ± 0.198	6.23 ± 4.95	25.88 ± 22.43
+ Difficulty-Aware Sampling	0.816 ± 0.117	0.804 ± 0.136	0.83 ± 0.125	5.98 ± 4.52	18.72 ± 16.91
4. + Composite Loss(Complete)	0.831 ± 0.093	0.816 ± 0.105	0.84 ± 0.107	3.03 ± 2.25	13.46 ± 12.44

Note: All experiments conducted with fixed SYNAPSE-Net architecture. Performance metrics demonstrate incremental improvements with each added pipeline component.

the mathematical formulation is given by:

$$\begin{aligned} \text{HD95}(Y, \hat{Y}) &= \max \left(\mathcal{P}_{95} \left\{ \min_{b \in \partial Y} ||a - b|| \ \forall a \in \partial \hat{Y} \right\}, \\ \mathcal{P}_{95} \left\{ \min_{a \in \partial \hat{Y}} ||b - a|| \ \forall b \in \partial Y \right\} \right) \end{aligned} \tag{38}$$

The Absolute Volume Difference (AVD) quantifies the percentage error in the predicted lesion volume:

$$AVD(\%) = \frac{|V_{gt} - V_{pred}|}{V_{gt}} \times 100\%$$
 (39)

3.4.2. Object-Level (Lesion-Based) Metrics

Object-level metrics evaluate the detection of individual lesions, which we identify using 3D connected-component analysis. Lesion Recall measures the fraction of true lesions detected:

$$Recall_{L} = \frac{N_{TP_{L}}}{N_{TP_{L}} + N_{FN_{L}}}$$
 (40)

The Lesion F1-Score provides a balanced measure of detection performance, combining precision and recall:

$$F1_{L} = \frac{2 \cdot N_{TP_{L}}}{2 \cdot N_{TP_{L}} + N_{FP_{L}} + N_{FN_{L}}}$$
(41)

These object-level metrics are crucial for tasks like WMH segmentation, where failing to detect a single small lesion is a significant clinical error. Looking at (37) - (41), we can see that higher scores in DSC, lesion recall, and F1 indicate better segmentation. On the other hand, lower HD95 and AVD values signify more accurate results, as they reflect smaller boundary and volume errors.

3.5. Quantitative Analysis of Ablation Studies

In order to effectively deconstruct the role of the proposed framework, a comprehensive evaluation was performed on the WMH dataset using three specific analyses. Among these were ablation studies associated with the training pipeline and structural architecture, followed by a design rationale study that validated the 2D architectural principle. The quantitative findings from these analyses have been discussed in Tables 3, 4, and 5. Fig. 6 provides a better understanding in terms of performance consistency for specific experimental settings.

3.5.1. Ablation Study of the Training Pipeline

This work experimentally evaluates the effect of our training protocols while keeping the structure of the SYNAPSE-Net constant. The results are discussed in Table 3.

The baseline model (1) minimal pipeline using standard minmax normalization combined with an ordinary BCE+Dice loss function, established the initial performance. However, this result was compromised by significant variability and a comparatively bigger boundary error, which indicates a lack of edge localization. Subsequently, we assessed the impact of (2) robust preprocessing with Z-score normalization. This adjustment resulted in an instantaneous enhancement across all metrics, evidenced by both overlap and volumetric accuracy. Furthermore, the standard deviation of the DSC also reduced, indicating more stable performance. Then, we applied our (3) difficulty-aware sampling technique. As displayed in Table 3, the resulting methodology led to an observable improvement in object-level detection, as lesion recall increased from 0.72 to 0.83. This is direct evidence for the efficacy of the technique in correcting severe slice-level class imbalance. Finally, the (4) full framework introduced our combined Focal-Tversky loss with Boundary loss. This stage achieved the highest overall performance. The noticeable improvement was seen in boundary overlap metrics. This marks the significance of the Boundary loss function for achieving the highest geometric fidelity and the Focal-Tversky loss for gaining region overlap and recall, which are testimonies of the synergistic benefit of combining all proposed pipeline components.

3.5.2. Ablation Study of Architectural Components

The next study evaluated the effects of our novel architectural components, using the complete training pipeline on each model. The quantitative findings are shown in Table 4 and qualitative examples provided in Fig. 5.

Our baseline (1), a standard UNet++, had a satisfactory DSC, but its large HD95 value and its instability clearly reflect its weaknesses in precision. The qualitative results in Fig. 5 are typical where the baseline model detects larger lesions but has noisy poorly defined borders and severe under-segmentation, especially for small lesions. Next, we evaluated the influence of our (2) advanced bottleneck that incorporates the multi-stream encoders, Swin Transformers, and the CMAF module. This addition resulted in a substantial boost in performance in a way that the mean DSC and the HD95 improved significantly. The reason for this improvement lies in the ability of the Swin Transformer in characteristic modeling of long-range spatial context as well as the intelligent multi-modal fusion capability of the CMAF module. Finally, the (3) full SYNAPSE-Net was assessed, which integrated our novel hierarchical gated decoder. The highest improvement was again noted in the HD95 measure, reducing by around 40%. This provides conclusive proof that hierarchical gating mechanism plays a significant role in

Table 4: Architectural Ablation Study on WMH Dataset

Model Configuration	DSC↑	Lesion F1 ↑	Lesion Recall ↑	HD95 ↓	AVD ↓
1. Baseline (Standard UNet++)	0.772 ± 0.145	0.75 ± 0.170	0.80 ± 0.161	7.15 ± 5.88	23.41 ± 20.15
+ Advanced Bottleneck	0.819 ± 0.112	0.796 ± 0.128	0.82 ± 0.130	4.88 ± 3.91	16.85 ± 15.02
Full SYNAPSE-Net	0.831 ± 0.093	0.816 ± 0.105	0.84 ± 0.107	3.03 ± 2.25	13.46 ± 12.44

Note: All models trained using the complete, optimized training pipeline.

Table 5: Quantitative Comparison Between 2D and 3D SYNAPSE-Net Variants (n=30)

Variant	DSC ↑	Recall ↑	HD95 ↓	Signif.	Params (M)	Patch FLOPs (G)	Full FLOPs (G)
2D	0.607 ± 0.25	0.56 ± 0.28	31.47 ± 12.52	p > 0.05	13.52	13.12	138.6
3D	0.609 ± 0.32	0.57 ± 0.21	32.26 ± 15.17	p > 0.05	33.36	1,753.8	60,177

Note: Paired t-tests revealed no significant differences (Dice: t(29)=0.076, p=0.94; Recall: t(29)=0.427, p=0.67; HD95: t(29)=0.652, p=0.52). FLOPs computed on 64×64 (2D) and $64\times64\times64$ (3D) patches, then extrapolated to full 208×208 input.

achieving excellent geometric fidelity. By implementing high-level semantic features as a means of modulating the passage of low-level spatial information, the decoder defines intricate lesion borders more accurately. This finding is evident visually in Fig. 5, where the full model produces the finest boundaries with an ability to detect small subtle lesions missed by preceding frameworks. Additionally, as evident from the boxplots in Fig. 6, the standard deviation of all metrics reached their lowest points, demonstrating that the complete architecture is the most robust and reliable.

3.5.3. Design Rationale: 2D vs. 3D Architecture

To find out which dimensionality is the most suitable for brain lesion segmentation, a direct comparison between 2D and 3D SYNAPSE-Net variants was carried out under identical conditions. For both models, a batch size of 4 was used, while eval-

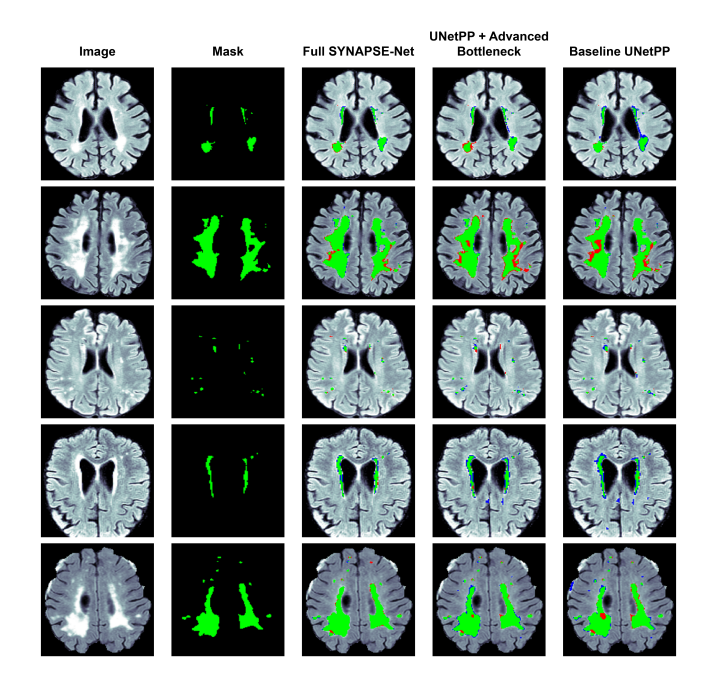


Figure 5: Qualitative results of the architectural ablation study on the WMH dataset. Segmentation overlays show true positives (green), false negatives (red), and false positives (blue).

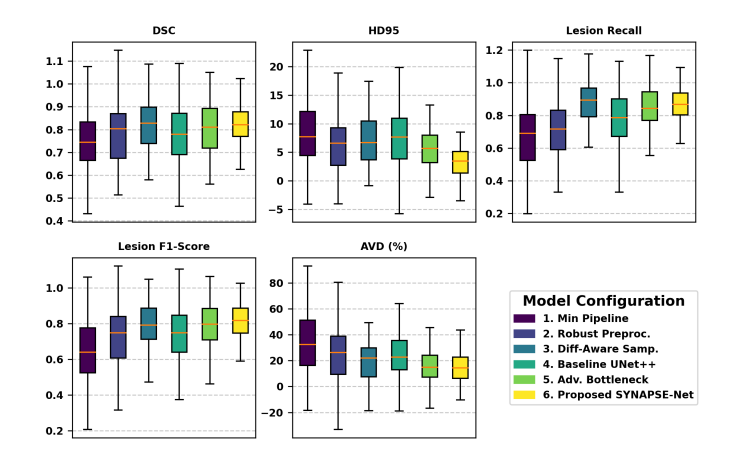


Figure 6: Boxplot visualization of key performance metrics from ablation studies.

uation was performed on a representative subset of 30 patients from the WMH dataset of full resolution 3D volumes.

Because of GPU memory constraints, computational metrics were evaluated for smaller input sizes for 2D (' 64×64 ') and 3D (' $64 \times 64 \times 64$ ') images, which were then scaled up to ' 208×208 ' by factors of $(208/64)^2 = 10.56$ for 2D images and $(208/64)^3 = 34.33$ for 3D images. Statistical significance was calculated by paired t-tests on subject-wise Dice, Recall, and HD95 values.

As seen in Table 5, both models had almost equal performance on every parameter, with no significant difference statistically (p > 0.05) between the two models. But the computational cost of the 3D model was much more, with FLOPs over $430\times$ that of the 2D model. With equivalent accuracy but with vastly lower computational requirements, it was decided that for all main experiments, a 2D configuration would be employed ensuring scalability and deployment efficiency without compromising segmentation quality.

3.6. Comparison with State-of-the-Art Methods

To contextualize the performance of our unified framework, we benchmarked the SYNAPSE-Net against a range of leading, specialized methods on each of the three datasets.

Table 6: Performance Comparison on the MICCAI WMH 2017 Dataset

Network	Code Avail.	DSC ↑	F 1 ↑	Recall ↑	AVD \downarrow	HD95 ↓	Parameters
Ensemble HFU-Net (Park et al., 2021)	✓	0.81*	0.79*	0.82*	18.58*	5.63*	8.5M
FCN Ensembles (Li et al., 2018)	✓	0.80^{*}	0.76^{*}	0.84^{*}	21.88^*	6.30^{*}	8.8M
Swin U-Net (Viteri et al., 2022)	✓	0.80^{*}	0.63^{*}	0.72^{*}	16.93*	3.16+	28.8M
Skip Connection U-Net (Wu et al., 2019)	✓	0.7836^{*}	0.7086^*	0.8149^{*}	28.23^{*}	7.36^{*}	10.56M
Attention SwinU-Net (He et al., 2025)	Х	0.72^{*}	N/A	0.92^{*}	50*	9.47^{*}	N/A
WMH-DualTasker (Wu et al., 2025)	Х	0.602^{*}	0.677^{*}	0.758^{*}	33.8^{*}	N/A	N/A
CRF U-Net (Zhou et al., 2020)	Х	0.78^{*}	0.67^{*}	0.77^{*}	10^*	3.70^{*}	N/A
V-Net (Huang et al., 2023)	Х	0.75^{*}	0.72^{*}	0.61*	30.6*	6.04^{*}	N/A
SegAE (Atlason et al., 2019)	Х	0.62^{*}	0.36^{*}	0.33^{*}	44.19*	24.49^*	N/A
ResU-net (Jin et al., 2018)	✓	0.75^{*}	0.69^{*}	0.81*	27.26^{*}	7.35*	28.86M
SYNAPSE-Net (ours)		0.831	0.816	0.84	13.46	3.03	13.46M

Note: Bold indicates the best performance for each metric. Code Availability indicates if the method's code was publicly available for qualitative comparison. N/A indicates parameter count not available

Statistical significance of differences from our model, obtained using paired two-tailed t-tests at a 95% confidence level, is denoted as follows: (*) for p < 0.05 (statistically significant) and (+) for p > 0.05 (not significant).

Table 7: Performance Comparison on the ISLES 2022 Dataset

Network	DSC↑	F 1 ↑	Recall ↑	HD95 ↓	Parameters
nnU-Net	0.6982*	0.6567*	0.5981*	27.55*	24.31 M
ResU-Net	0.7207^*	0.7385^{+}	0.6691*	15.77*	28.86 M
UNETR	0.6342^{*}	0.5953*	0.5247^*	37.16 [*]	42.47 M
Swin UNETR	0.6627^{*}	0.6213^*	0.5636^*	28.30^{*}	33.63 M
Ensemble UNet	0.7580^{+}	0.7088^{*}	0.7212^{*}	14.59*	8.8 M
DenseNet	0.6423*	0.6019^{*}	0.5741*	34.38*	17.94 M
SYNAPSE-Net (ours)	0.7632	0.7420	0.7056	9.69	13.46 M

Note: Bold indicates the best performance for each metric. Statistical significance of differences from our model, obtained using paired two-tailed t-tests at a 95% confidence level, is denoted as follows: (*) for p < 0.05 (statistically significant) and (+) for p > 0.05 (not significant).

3.6.1. WMH Segmentation Performance

We experimented SYNAPSE-Net on MICCAI 2017 WMH data for comparison with ten state-of-the-art models. In Table 6, the quantitative results demonstrate that our proposed framework achieves a superior and more balanced performance profile across all key evaluation metrics.

Our network achieved the highest DSC of 0.831 and lesion F1-score of 0.816, indicating a superior balance of precision and recall at both the voxel and object levels. Our model's DSC was significantly higher than the best ensemble methods like Ensemble HFU-Net (Park et al., 2021) and FCN Ensembles (Li et al., 2018). Though CRF U-Net (Zhou et al., 2020) had the highest %AVD, our network's %AVD of 13.46 was highly competitive and paired with much stronger overlap and detection scores, suggesting a more accurate and reliable estimation of the total lesion burden. The most significant advantage of our framework is highlighted by its exceptional performance on boundary awareness. As detailed in Table 6, our model gets the best HD95 score of 3.03. It significantly outperforms the majority of methods (e.g., by over 50% compared to 7.35 of ResU-Net (Jin et al., 2018)) as well as performs comparably to 3.16 of Swin U-Net (Viteri et al., 2022). This quantitative superiority in boundary adherence is visually substantiated in Fig. 7. In the instances of big, confluent lesions (row 3 and 5), methods like ResU-Net and SCU-Net (Wu et al., 2019) display under-segmentation as well as poorly estimated edges, so their bigger HD95 values.

Our proposed framework demonstrates robust lesion detection with 0.84 recall. Though Attention SwinU-Net (He et al., 2025) achieved a higher recall of 0.92, this came at the

cost of a lower DSC of 0.72, indicating a tendency for oversegmentation. Our SYNAPSE-Net, however, achieves its high recall while maintaining the highest DSC which proves the ability of our model to find the vast majority of lesions without sacrificing segmentation accuracy. Furthermore, SYNAPSE-Net delivers this state-of-the-art performance with a lean 13.46M parameters, making it more efficient than other high-performing models such as Swin U-Net (28.8M).

It is visual in rows of small lesions (row 1 and 4 of Fig. 7), where our system identifies almost all the small satellite lesions, in contrast to those of competing methods like Ensemble HFU-Net and FCN Ensembles. Such detection robustness as well as higher boundary detection competency in Table 6 validate our

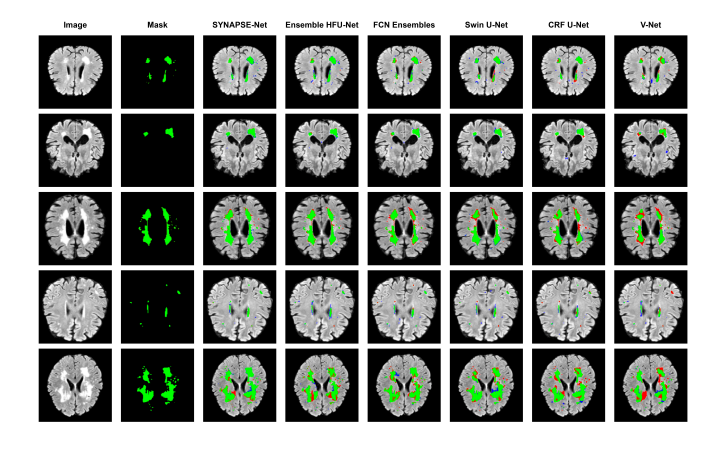


Figure 7: Qualitative comparison on the WMH test set. Green (True Positive), Red (False Negative/Missed Lesion), Blue (False Positive/Over-segmentation).

method's performance for WMH segmentation.

3.6.2. Ischemic Stroke Segmentation Performance

We evaluated our framework's performance on acute vascular lesions against several strong baselines and state-of-the-art models. Table 7 compares our approach against several established methods: nnU-Net (Isensee et al., 2020), ResU-Net (Jin et al., 2018), the transformer-based UNETR (Hatamizadeh et al., 2021) and Swin UNETR (Hatamizadeh et al., 2022) architectures, along with the Ensemble UNet (Li et al., 2018).

Our evaluation shows SYNAPSE-Net delivering top-tier performance, securing the best DSC (0.7632) and F1 (0.7420) results. Ensemble UNet maintains a competitive DSC score (0.7580) that does not differ significantly from ours, but its F1 performance (0.7088) now falls significantly short. ResU-Net presents improved F1 (0.7385) although it is not statistically different from our model, while its DSC (0.7207) remains substantially lower. Our framework's most substantial advantage appears in boundary accuracy. The model achieved an HD95 of 9.69, surpassing Ensemble UNet (14.59) by 33.6% and ResU-Net (15.77) by 38.6%. This clear margin confirms that our hierarchical gated decoder and cross-modal fusion mechanism excel at producing geometrically precise segmentations. Besides, SYNAPSE-Net delivers this leading performance with only 13.46M parameters, demonstrating better efficiency than larger models like ResU-Net (28.86M) and UNETR (42.47M), while outperforming the more compact Ensemble UNet (8.8M) in crucial boundary-aware metrics.

This advantage in boundary accuracy is shown in Fig. 8. In the case of large and complex infarcts (rows 1 and 4), models such as Swin UNETR and DenseNet (Huang et al., 2017) exhibit under-segmentation along gyral boundaries, which is reflected in their unsatisfactory HD95 scores. Conversely, our model generates a precise segmentation that closely aligns with the ground truth. The second and third rows illustrate smaller, more subtle cortical and subcortical strokes where other models encounter difficulties. For example, although Ensemble UNet achieves a high recall, it produces scattered false positives. In contrast, our model yields a clean and precise segmentation

with minimal errors. The final row, representing a challenging cerebellar stroke, further highlights the precision of our model. In this instance, models like DenseNet and ResU-Net encounter substantial segmentation inaccuracies, whereas our framework successfully delineates the lesion.

3.6.3. Brain Tumor Segmentation Performance

In the context of pre-surgical glioma separation, SYNAPSE-Net was benchmarked on the BraTS 2020 data set for comparison on par with the best CNN-based (e.g., nnU-Net) and Transformer-based (e.g., TransBTS) models. The quantitative results for the Whole Tumor (WT), Tumor Core (TC), and Enhancing Tumor (ET) sub-regions are detailed in Table 8. Our proposed framework achieved highly competitive and state-ofthe-art performance. In terms of the WT, the DSC of 0.91 achieved by our model is statistically comparable to leading methodologies such as nnU-Net (Isensee et al., 2020). The principal advantage of our framework is its efficacy in segmenting the more intricate sub-regions. As shown in Table 8, our model attains the highest DSC for the TC at 0.87 and the most favorable HD95 for both TC and the ET. These enhancements are statistically significant, reflecting an enhanced capacity for accurately delineating complex tumor boundaries. SYNAPSE-Net delivers this top-tier performance while remaining highly parameter-efficient (28.62M), especially when compared to larger architectures also listed in the table.

The quantitative superiority is illustrated visually in Fig. 9. For instance, considering for the large, irregular tumor (row 1), our network provides an artifact-free segmentation, unlike TransBTS (Wang et al., 2021) and DR-UNet (Colman et al., 2021), which show significant misclassifications. In row 2, our method accurately encompasses the whole hyperintensity without generating more false negatives as compared to some other models like AD-Net (Peng and Sun, 2023). Also, on challenging cases with complex enhancing patterns (rows 3 and 4), our model shows a more accurate delineation of the enhancing tumor with less leakage than nnU-Net and SaE-Net (Iantsen et al., 2021). Such robust and precise performance on all three tumor sub-regions validates the effectiveness of our framework in han-

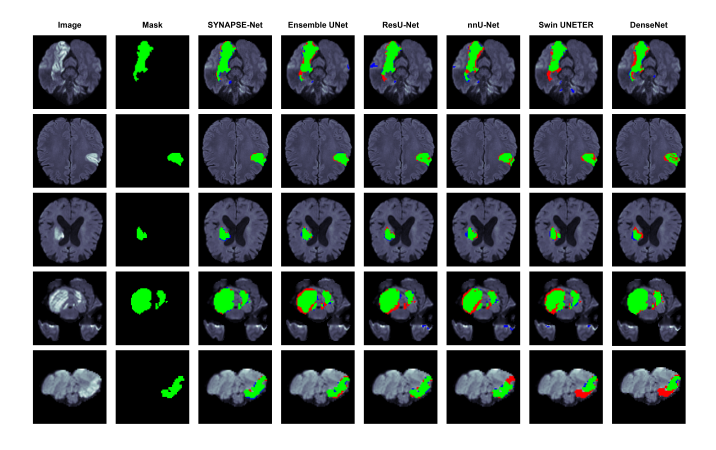


Figure 8: Qualitative comparison on the ISLES 2022 dataset. Green (True Positive), Red (False Negative), Blue (False Positive).

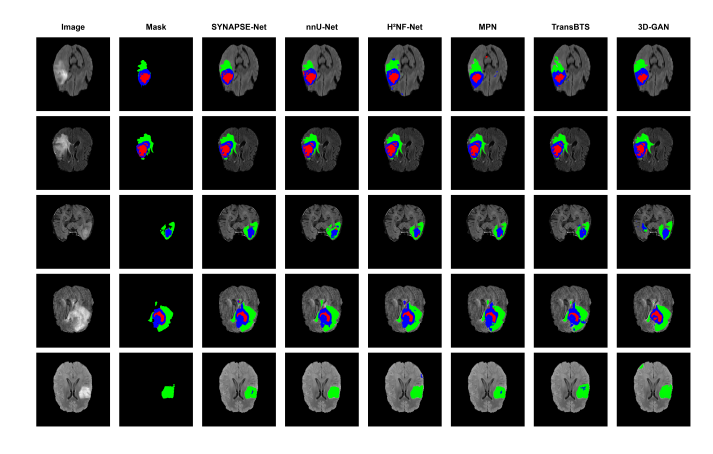


Figure 9: Qualitative comparison on the BraTS 2020 dataset. Tumor Sub-Regions: Green (Whole Tumor), Red (Tumor Core), Blue (Enhancing Tumor).

Table 8: Performance Comparison on the BraTS20 Dataset

Network	Code Avail.		DSC ↑			HD95 ↓		Parameters
		WT	TC	ET	WT	TC	ET	
nnU-net (Isensee et al., 2020)	1	0.912*	0.857*	0.799*	3.73*	5.64*	26.41*	101.88 M
AD-Net (Peng and Sun, 2023)	✓	0.900^{*}	0.800^{*}	0.760^{*}	7.22*	15.30*	35.20*	5.27 M
MPN (Wang et al., 2020)	X	0.908^{+}	0.856^{+}	0.787^{+}	4.71*	5.70*	35.01*	N/A
DR-Unet (Colman et al., 2021)	✓	0.886*	0.669*	0.655*	18.39*	53.61*	16.19*	76.5 M
3D-GAN (Cirillo et al., 2020)	X	0.893*	0.792*	0.750^{*}	6.39*	14.07*	36.00*	N/A
MultiResUNet (Tang et al., 2021)	X	0.893*	0.790^{*}	0.703*	4.63*	10.07*	34.31*	N/A
DLA (Silva et al., 2021)	X	0.905^{+}	0.789^*	0.725^*	8.06*	8.93*	33.87*	N/A
SaE-Net (Iantsen et al., 2021)	✓	0.887*	0.843*	0.805^{*}	4.54*	19.59*	15.43*	37.59 M
TransBTS (Wang et al., 2021)	✓	0.901+	0.817*	0.787+	4.96*	9.77*	17.95*	32.99 M
SYNAPSE-Net (ours)		0.906	0.865	0.788	4.32	4.34	10.94	41.32 M

Note: Bold indicates the best performance for each metric. Code Availability indicates if the method's code was publicly available for qualitative comparison. N/A indicates parameter count not available.

Statistical significance of differences from our model, obtained using paired two-tailed t-tests at a 95% confidence level, is denoted as follows: (*) for p < 0.05 (statistically significant) and (+) for p > 0.05 (not significant).

dling the heterogeneity of glioblastoma.

4. Limitations and Future Works

Although the proposed framework performs well on a variety of challenges, it has some drawbacks that suggest important areas for further study. One of the considerable limitation is the hierarchical fusion strategy for the 4-modality BraTS task which depends on a pre-defined, heuristic-based pairing of modalities. The next logical step would be to develop an end-to-end fully learnable grouping mechanism. Furthermore, although our use of post-hoc grid search for binarization thresholding is effective, it might be improved by integrating model uncertainty estimates directly into the inference procedure itself. Additionally, even though our 2D method has demonstrated both computational efficiency and high efficacy across a variety of lesion types, there is still room for exciting research into how to incorporate 3D contextual information, especially for pathologies where volumetric relationships are clinically critical. By addressing these issues and extending the framework's applicability to an even wider range of neurological conditions, we intend to build on this work.

5. Conclusion

In this work, we addressed two main challenges of automated medical image segmentation: lack of generalization between pathologies and high variability in performance for existing models. We propose the unified multi-stream SYNAPSE-Net, a CNN-Transformer hybrid architecture providing an effective solution for both challenges. The core of our contribution is proposing a 'unified but adaptable' methodology that incorporate a robust architectural design involving multi-stream encoding, a hybrid bottleneck using Swin Transformers, crossmodal attention, and hierarchical gated decoder with an adaptable training pipeline adapted to the unique characteristics of each clinical task.

The SYNAPSE-Net was validated on three distinct public datasets, showing top performance in each. For the MICCAI 2017 WMH dataset, it achieved the highest DSC of 0.831 and

the best boundary metric HD95 of 3.03, showing effective segmentation in small lesions. On the ISLES 2022 dataset, it attained a state-of-the-art HD95 score of 9.69, demonstrating its superior design for complex acute ischemic stroke lesions. Lastly, on the BraTS 2020 dataset, it performed effectively to segment the critical sub-regions of the Tumor Core (TC) and Enhancing Tumor (ET) demonstrating its capability in a multiclass, quad-modality context.

This study shows that a single, generalizable framework can achieve state-of-the-art performance across different pathologies, moving beyond the 'point solutions' that currently dominate the literature. Our ablation studies experimentally verified our key components quantitatively. The pipeline ablation reproduced our variance-reduction approach successfully, demonstrating difficulty-aware sampling, composite loss, and robust preprocessing as crucial components for stability. The architecture ablation verified the low-resolution feature extraction capability of hybrid bottleneck and geometric precision preserving quality of hierarchical gated decoder.

CRediT authorship contribution statement

Md. Mehedi Hassan: Writing - original draft, Writing - review & editing, Visualization, Validation, Software, Resources, Project administration, Methodology, Investigation, Funding acquisition, Formal analysis, Data curation, Conceptualization.

Shafqat Alam: Writing - original draft, Writing - review & editing, Visualization, Validation, Software, Resources, Methodology, Investigation, Formal analysis, Data curation, Conceptualization.

Shahriar Ahmed Seam: Writing - review & editing, Visualization, Validation, Software, Methodology, Investigation, Formal analysis, Data curation, Conceptualization.

Maruf Ahmed: Writing - review & editing, Supervision, Resources, Project administration, Funding acquisition, Formal analysis, Investigation.

Declaration of competing interest

The authors declare that they have no known competing financial interests or personal relationships that could have appeared to influence the work reported in this paper.

Acknowledgments

This work was partially supported by the Basic Research Grant from Bangladesh University of Engineering and Technology (BUET).

Data Availability

Links to the source code and the public datasets used in this study are provided in the manuscript.

Appendix: Supplementary Material

High-resolution inference results on the test sets for all evaluated datasets are provided as supplementary materials and can be accessed via the following link: https://tinyurl.com/5btu27ud

References

- Abbaoui, W., Retal, S., Ziti, S., El Bhiri, B., 2024. Automated ischemic stroke classification from MRI scans: Using a vision transformer approach. Journal of Clinical Medicine 13, 2323. doi:10.3390/jcm13082323.
- Ates, G.C., Mohan, P., Celik, E., 2023. Dual cross-attention for medical image segmentation. arXiv preprint arXiv:2303.17696. doi:10.48550/ARXIV.2303.17696.
- Atlason, H.E., Love, A., Sigurdsson, S., Gudnason, V., Ellingsen, L.M., 2019. SegAE: Unsupervised white matter lesion segmentation from brain MRIs using a CNN autoencoder. NeuroImage: Clinical 24, 102085. doi:10.1016/j.nicl.2019.102085.
- Ayoub, M., Liao, Z., Hussain, S., Li, L., Zhang, C.W.J., Wong, K.K.L., 2023. End to end vision transformer architecture for brain stroke assessment based on multi-slice classification and localization using computed tomography. Computerized Medical Imaging and Graphics 109, 102294. doi:10.1016/j.compmedimag.2023.102294.
- Azad, R., et al., 2024. Medical image segmentation review: The success of U-Net. IEEE Transactions on Pattern Analysis and Machine Intelligence 46, 10076–10095. doi:10.1109/TPAMI.2024.3435571.
- Bakas, S., et al., 2017. Advancing the cancer genome atlas glioma MRI collections with expert segmentation labels and radiomic features. Scientific Data 4, 170117. doi:10.1038/sdata.2017.117.
- Bakas, S., et al., 2018. Identifying the best machine learning algorithms for brain tumor segmentation, progression assessment, and overall survival prediction in the BRATS challenge. arXiv preprint arXiv:1811.02629. doi:10.48550/ARXIV.1811.02629.

- Barber, R., et al., 1999. White matter lesions on magnetic resonance imaging in dementia with Lewy bodies, Alzheimer's disease, vascular dementia, and normal aging. Journal of Neurology, Neurosurgery & Psychiatry 67, 66–72. doi:10.1136/jnnp.67.1.66.
- Cabezas, M., Diez, Y., 2024. An analysis of loss functions for heavily imbalanced lesion segmentation. Sensors 24, 1981. doi:10.3390/s24061981.
- Capirossi, C., Laiso, A., Renieri, L., Capasso, F., Limbucci, N., 2023. Epidemiology, organization, diagnosis and treatment of acute ischemic stroke. European Journal of Radiology Open 11, 100527. doi:10.1016/j.ejro.2023.100527.
- Chaki, J., Woźniak, M., 2023. Deep learning for neurodegenerative disorder (2016 to 2022): A systematic review. Biomedical Signal Processing and Control 80, 104223. doi:10.1016/j.bspc.2022.104223.
- Chau, M., Vu, H., Debnath, T., Rahman, M.G., 2025. A scoping review of automatic and semi-automatic MRI segmentation in human brain imaging. Radiography 31, 102878. doi:10.1016/j.radi.2025.01.013.
- Chen, J., et al., 2024. TransUNet: Rethinking the U-Net architecture design for medical image segmentation through the lens of transformers. Medical Image Analysis 97, 103280. doi:10.1016/j.media.2024.103280.
- Chen, Y.T., et al., 2025. Automatic segmentation of white matter lesions on multi-parametric MRI: convolutional neural network versus vision transformer. BMC Neurology 25, 5. doi:10.1186/s12883-024-04010-6.
- Cirillo, M.D., Abramian, D., Eklund, A., 2020. Vox2Vox: 3D-GAN for brain tumour segmentation. arXiv preprint arXiv:2003.13653. doi:10.48550/ARXIV.2003.13653.
- Colman, J., Zhang, L., Duan, W., Ye, X., 2021. DR-Unet104 for multimodal MRI brain tumor segmentation, in: Crimi, A., Bakas, S. (Eds.), Brainlesion: Glioma, Multiple Sclerosis, Stroke and Traumatic Brain Injuries, Springer International Publishing, Cham. pp. 410–419. doi:10.1007/978-3-030-72087-2_36.
- Demeusy, V., et al., 2024. Development and validation of a twostage convolutional neural network algorithm for segmentation of MRI white matter hyperintensities for longitudinal studies in CADASIL. Computers in Biology and Medicine 180, 108936. doi:10.1016/j.compbiomed.2024.108936.
- Du, L., Wang, L., Shen, G., Zeng, M., Li, D., Li, W., 2025. Progress of radiomics research on white matter hyperintensity lesions. Frontiers in Neurology 16, 1647724. doi:10.3389/fneur.2025.1647724.
- Duarte, K.T.N., et al., 2024. Multi-stage semi-supervised learning enhances white matter hyperintensity segmentation. Frontiers in Computational Neuroscience 18, 1487877. doi:10.3389/fncom.2024.1487877.

- Gaubert, M., et al., 2023. Performance evaluation of automated white matter hyperintensity segmentation algorithms in a multicenter cohort on cognitive impairment and dementia. Frontiers in Psychiatry 13, 1010273. doi:10.3389/fpsyt.2022.1010273.
- Gheibi, Y., Shirini, K., Razavi, S.N., Farhoudi, M., Samad-Soltani, T., 2023. CNN-Res: deep learning framework for segmentation of acute ischemic stroke lesions on multimodal MRI images. BMC Medical Informatics and Decision Making 23, 192. doi:10.1186/s12911-023-02289-y.
- Grochans, S., et al., 2022. Epidemiology of Glioblastoma Multiforme–Literature Review. Cancers 14, 2412. doi:10. 3390/cancers14102412.
- Hatamizadeh, A., Nath, V., Tang, Y., Yang, D., Roth, H., Xu, D., 2022. Swin UNETR: Swin transformers for semantic segmentation of brain tumors in MRI images. arXiv preprint arXiv:2201.01266. doi:10.48550/ARXIV.2201.01266.
- Hatamizadeh, A., Tang, Y., Nath, V., Yang, D., Myronenko, A., Landman, B., Roth, H., Xu, D., 2021. UNETR: Transformers for 3D Medical Image Segmentation. URL: https://arxiv.org/abs/2103.10504, doi:10.48550/ARXIV.2103.10504. version Number: 3.
- He, H., et al., 2025. A robust automated segmentation method for white matter hyperintensity of vascular-origin. NeuroImage 315, 121279. doi:10.1016/j.neuroimage.2025. 121279.
- Hernandez Petzsche, M.R., et al., 2022. ISLES 2022: A multi-center magnetic resonance imaging stroke lesion segmentation dataset. Scientific Data 9, 762. doi:10.1038/s41597-022-01875-5.
- Huang, F., et al., 2023. Semisupervised white matter hyperintensities segmentation on MRI. Human Brain Mapping 44, 1344–1358. doi:10.1002/hbm.26109.
- Huang, G., Liu, Z., Van Der Maaten, L., Weinberger, K.Q., 2017. Densely Connected Convolutional Networks, in: 2017 IEEE Conference on Computer Vision and Pattern Recognition (CVPR), IEEE, Honolulu, HI. pp. 2261–2269. URL: https://ieeexplore.ieee.org/ document/8099726/, doi:10.1109/CVPR.2017.243.
- Iantsen, A., Jaouen, V., Visvikis, D., Hatt, M., 2021. Squeeze-and-excitation normalization for brain tumor segmentation, in: Crimi, A., Bakas, S. (Eds.), Brainlesion: Glioma, Multiple Sclerosis, Stroke and Traumatic Brain Injuries, Springer International Publishing, Cham. pp. 366–373. doi:10.1007/978-3-030-72087-2_32.
- Isensee, F., Jaeger, P.F., Full, P.M., Vollmuth, P., Maier-Hein, K.H., 2020. nnU-Net for brain tumor segmentation. arXiv preprint arXiv:2011.00848. doi:10.48550/ARXIV.2011.00848.

- Jenkinson, M., Beckmann, C.F., Behrens, T.E.J., Woolrich, M.W., Smith, S.M., 2012. FSL. NeuroImage 62, 782–790. doi:10.1016/j.neuroimage.2011.09.015.
- Jin, D., Xu, Z., Harrison, A.P., Mollura, D.J., 2018. White matter hyperintensity segmentation from T1 and FLAIR images using fully convolutional neural networks enhanced with residual connections, in: 2018 IEEE 15th International Symposium on Biomedical Imaging (ISBI 2018), IEEE, Washington, DC. pp. 1060–1064. doi:10.1109/ISBI.2018.8363754.
- Johnson, D.R., 2012. Rising incidence of glioblastoma and meningioma in the united states: Projections through 2050. Journal of Clinical Oncology 30, 2065–2065. doi:10.1200/ jco.2012.30.15_suppl.2065.
- Kervadec, H., Bouchtiba, J., Desrosiers, C., Granger, E., Dolz, J., Ayed, I.B., 2018. Boundary loss for highly unbalanced segmentation. arXiv preprint arXiv:1812.07032. doi:10.48550/ARXIV.1812.07032.
- Kuijf, H., et al., 2022. Data of the white matter hyperintensity (WMH) segmentation challenge. doi:10.34894/AECRSD.
- Li, H., et al., 2018. Fully convolutional network ensembles for white matter hyperintensities segmentation in MR images. NeuroImage 183, 650–665. doi:10.1016/j.neuroimage. 2018.07.005.
- Li, X., et al., 2024. Global, regional, and national burden of ischemic stroke, 1990–2021: an analysis of data from the global burden of disease study 2021. eClinicalMedicine 75, 102758. doi:10.1016/j.eclinm.2024.102758.
- Liu, J., et al., 2025. Epidemiology and future trend predictions of ischemic stroke based on the global burden of disease study 1990–2021. Communications Medicine 5, 273. doi:10.1038/s43856-025-00939-y.
- Liu, Z., et al., 2021. Swin transformer: Hierarchical vision transformer using shifted windows. arXiv preprint arXiv:2103.14030. doi:10.48550/ARXIV.2103.14030.
- Luo, J., Dai, P., He, Z., Huang, Z., Liao, S., Liu, K., 2024. Deep learning models for ischemic stroke lesion segmentation in medical images: A survey. Computers in Biology and Medicine 175, 108509. doi:10.1016/j.compbiomed. 2024.108509.
- Menze, B.H., et al., 2015. The multimodal brain tumor image segmentation benchmark (BRATS). IEEE Transactions on Medical Imaging 34, 1993–2024. doi:10.1109/TMI.2014. 2377694.
- Namgung, E., et al., 2025. Deep learning to identify stroke within 4.5 h using DWI and FLAIR in a prospective multicenter study. Scientific Reports 15, 26262. doi:10.1038/s41598-025-10804-6.

- Park, G., Hong, J., Duffy, B.A., Lee, J.M., Kim, H., 2021. White matter hyperintensities segmentation using the ensemble U-Net with multi-scale highlighting foregrounds. NeuroImage 237, 118140. doi:10.1016/j.neuroimage.2021. 118140.
- Peng, Y., Sun, J., 2023. The multimodal MRI brain tumor segmentation based on AD-Net. Biomedical Signal Processing and Control 80, 104336. doi:10.1016/j.bspc.2022. 104336.
- Punn, N.S., Agarwal, S., 2022. Modality specific U-Net variants for biomedical image segmentation: a survey. Artificial Intelligence Review 55, 5845–5889. doi:10.1007/s10462-022-10152-1.
- R, P., M, J.P.P., S, N.J., 2025. Brain tumor segmentation using multi-scale attention U-Net with EfficientNetB4 encoder for enhanced MRI analysis. Scientific Reports 15, 9914. doi:10.1038/s41598-025-94267-9.
- Raju, C.S.P., Neelapu, B.C., Laskar, R.H., Muhammad, G., 2024. Analysis of multimodal fusion strategies in deep learning for ischemic stroke lesion segmentation on computed tomography perfusion data. Multimedia Tools and Applications 84, 7493–7518. doi:10.1007/s11042-024-19252-2.
- Ronneberger, O., Fischer, P., Brox, T., 2015. U-Net: Convolutional networks for biomedical image segmentation, in: Navab, N., Hornegger, J., Wells, W.M., Frangi, A.F. (Eds.), Medical Image Computing and Computer-Assisted Intervention MICCAI 2015, Springer International Publishing, Cham. pp. 234–241. doi:10.1007/978-3-319-24574-4_28.
- de la Rosa, E., et al., 2025. A robust ensemble algorithm for ischemic stroke lesion segmentation: Generalizability and clinical utility beyond the ISLES challenge. Nature Communications 16, 7357. doi:10.48550/arXiv.2403.19425.
- Sachdev, P.S., 2005. White matter hyperintensities are related to physical disability and poor motor function. Journal of Neurology, Neurosurgery & Psychiatry 76, 362–367. doi:10.1136/jnnp.2004.042945.
- Silva, C.A., Pinto, A., Pereira, S., Lopes, A., 2021. Multistage deep layer aggregation for brain tumor segmentation. arXiv preprint arXiv:2101.00490. doi:10.48550/ARXIV. 2101.00490.
- Sun, K., et al., 2024. CMAF-Net: a cross-modal attention fusion-based deep neural network for incomplete multimodal brain tumor segmentation. Quantitative Imaging in Medicine and Surgery 14, 4579–4604. doi:10.21037/qims-24-9.
- Takahashi, S., et al., 2024. Comparison of vision transformers and convolutional neural networks in medical image analysis: A systematic review. Journal of Medical Systems 48, 84. doi:10.1007/s10916-024-02105-8.

- Tang, J., Li, T., Shu, H., Zhu, H., 2021. Variational-autoencoder regularized 3D MultiResUNet for the BraTS 2020 brain tumor segmentation, in: Crimi, A., Bakas, S. (Eds.), Brainlesion: Glioma, Multiple Sclerosis, Stroke and Traumatic Brain Injuries, Springer International Publishing, Cham. pp. 431–440. doi:10.1007/978-3-030-72087-2_38.
- Tomasetti, L., et al., 2023. Self-supervised few-shot learning for ischemic stroke lesion segmentation. arXiv preprint arXiv:2303.01332. doi:10.48550/ARXIV.2303.01332.
- Tomita, N., Jiang, S., Maeder, M.E., Hassanpour, S., 2020. Automatic post-stroke lesion segmentation on MR images using 3D residual convolutional neural network. NeuroImage: Clinical 27, 102276. doi:10.1016/j.nicl.2020.102276.
- Vanderbecq, Q., et al., 2020. Comparison and validation of seven white matter hyperintensities segmentation software in elderly patients. NeuroImage: Clinical 27, 102357. doi:10.1016/j.nicl.2020.102357.
- Viteri, J.A., Piguave, B.V., Pelaez, E., Loayza, F.R., 2022. Automatic brain white matter hyperintensities segmentation with swin U-Net, in: 2022 IEEE ANDESCON, IEEE, Barranquilla, Colombia. pp. 1–6. doi:10.1109/ANDESCON56260.2022.9989775.
- Walsh, J., Othmani, A., Jain, M., Dev, S., 2022. Using U-Net network for efficient brain tumor segmentation in MRI images. Healthcare Analytics 2, 100098. doi:10.1016/j.health.2022.100098.
- Wang, W., Chen, C., Ding, M., Li, J., Yu, H., Zha, S., 2021. TransBTS: Multimodal brain tumor segmentation using transformer. arXiv preprint arXiv:2103.04430. doi:10. 48550/ARXIV.2103.04430.
- Wang, Y., et al., 2020. Modality-pairing learning for brain tumor segmentation. arXiv preprint arXiv:2010.09277. doi:10.48550/ARXIV.2010.09277.
- Woo, S., Park, J., Lee, J.Y., Kweon, I.S., 2018. CBAM: Convolutional block attention module. arXiv preprint arXiv:1807.06521. doi:10.48550/ARXIV.1807.06521.
- Wu, J., Zhang, Y., Wang, K., Tang, X., 2019. Skip connection U-Net for white matter hyperintensities segmentation from MRI. IEEE Access 7, 155194–155202. doi:10.1109/ACCESS.2019.2948476.
- Wu, Y., et al., 2025. WMH DualTasker: A weakly supervised deep learning model for automated white matter hyperintensities segmentation and visual rating prediction. Human Brain Mapping 46, e70212. doi:10.1002/hbm.70212.
- Wu, Z., Zhang, X., Li, F., Wang, S., Huang, L., Li, J., 2023. W-Net: A boundary-enhanced segmentation network for stroke lesions. Expert Systems with Applications 230, 120637. doi:10.1016/j.eswa.2023.120637.

- Yassin, M.M., et al., 2024. Advancing ischemic stroke diagnosis and clinical outcome prediction using improved ensemble techniques in DSC-PWI radiomics. Scientific Reports 14, 27580. doi:10.1038/s41598-024-78353-y.
- Zhang, G., Zhou, J., He, G., Zhu, H., 2023a. Deep fusion of multi-modal features for brain tumor image segmentation. Heliyon 9, e19266. doi:10.1016/j.heliyon.2023.e19266.
- Zhang, X., et al., 2023b. Self-supervised tumor segmentation with Sim2Real adaptation. IEEE Journal of Biomedical and Health Informatics 27, 4373–4384. doi:10.1109/JBHI. 2023.3240844.
- Zheng, P., Zhu, X., Guo, W., 2022. Brain tumour segmentation based on an improved U-Net. BMC Medical Imaging 22, 199. doi:10.1186/s12880-022-00931-1.
- Zhou, P., Liang, L., Guo, X., Lv, H., Wang, T., Ma, T., 2020. U-net combined with CRF and anatomical based spatial features to segment white matter hyperintensities, in: 2020 42nd Annual International Conference of the IEEE Engineering in Medicine & Biology Society (EMBC), IEEE, Montreal, QC, Canada. pp. 1754–1757. doi:10.1109/EMBC44109.2020.9175377.
- Zhou, Z., Siddiquee, M.M.R., Tajbakhsh, N., Liang, J., 2018. UNet++: A nested U-Net architecture for medical image segmentation. arXiv preprint arXiv:1807.10165. doi:10. 48550/ARXIV.1807.10165.